Monte Carlo Simulations of Large-Scale One-Dimensional Random Rough-Surface Scattering at Near-Grazing Incidence: Penetrable Case

Chi Hou Chan, Leung Tsang, *Fellow, IEEE*, and Qin Li

***Abstract*— Scattering from dielectric one-dimensional (1-D) random rough surfaces at near grazing incidence is studied for both TE and TM cases. To obtain accurate results at incidence angles of 80°–85°, we use long surface lengths of up to 1000 wavelengths. Numerical results are illustrated for dielectric surfaces corresponding to soil surfaces with various moisture contents. Results indicate that TM backscattering is much larger than that of TE backscattering. The ratio of TM to TE backscattering increases as a function of soil moisture and can be used as an indicator of soil moisture in remote sensing applications. However, the ratio of TM to TE backscattering is much lower than that predicted by the small perturbation method. To facilitate computation of scattering by such long surfaces, the previously developed banded-matrix iteration approach/canonical grid method (BMIA/CG) has been extended to dielectric surfaces. The numerical algorithm consists of translating the nonnear-field interaction to a flat surface and the interaction subsequently calculated by fast Fourier transform (FFT).**

***Index Terms*—Electromagnetic scattering, Monte Carlo methods, rough surfaces.**

I. Introduction

THE scattering of waves by random rough surfaces at low-grazing angles (LGA's) has important applications in remote sensing of oceans and land [1]–[3]. At such large angles of incidence, the shadowing effects are important, therefore, the classical Kirchhoff method is not applicable. The small perturbation method (SPM) has been used to analyze scattering for such a problem. New analytic methods such as the small slope approximation [4] have also been used. Recently, Monte Carlo simulations of direct solutions of the wave scattering problem have become a popular approach because of the advent of modern computers and the development of fast numerical methods. The most common method that has been used in numerical simulations is the integral equation method [5]–[13]. But at low grazing, the wave can go through multiple scattering on the surface. To simulate the phenomenon with Monte Carlo simulations thus requires a long surface. The use of a long surface means that there are large numbers of surface unknowns and a more powerful numerical method becomes necessary. Over the past few years, we have developed the banded-matrix iterative approach/canonical grid method (BMIA/CG) that permits the solution of large-scale random rough surface problems [14]–[18]. The essence of the method consists of decomposing the interaction into near- and nonnear-field interactions. The nonnear-field interactions are then expanded on a canonical grid, which is a horizontal surface in this case so that the fast Fourier transform (FFT) can be applied. The ability to solve a large surface problem allows us to tackle the near-grazing incidence problem [16], [18].

In this paper, we extend the method to treat scattering from dielectric one-dimensional (1-D) random rough surfaces at near grazing incidence. Both TE and TM cases are studied. Of particular interest is the ratio of TM to TE backscattering. It is well known that the small perturbation method predicts a large ratio of TM backscattering to TE backscattering [19]. In our numerical simulations, we illustrate results using surface lengths of up to 1000 wavelengths and incidence angles between 80 and 85°. The dielectric constants of the dielectric surface are chosen to simulate rough soil surfaces with varying soil moisture contents. Numerical results indicate that the ratio of TM to TE backscattering, though large, is at a much smaller value than that predicted by the small perturbation method. In Section II, we give the formulation of the integral equation. Two unknowns are required for each sample point on the penetrable surface. We use an incident wave that is tapered in its spectral domain. In Section III, we present the extension of the BMIA/CG method for the penetrable case. The nonnear-field interactions are computed simultaneously using FFT's upon a Taylor series expansion of Green's functions about a flat surface at the mean value of the surface height. Due to the presence of the extra set of unknowns $\partial\Psi/\partial n$, the banded matrix in the perfectly conducting case becomes four banded submatrices in the penetrable case. In Section IV, we illustrate numerical results of scattering of soil surfaces of various soil moisture contents up to a surface length of 1000 wavelengths for incidence angles between 80° and 85°. Backscattering coefficients of TM and TE waves for various soil moisture contents are tabulated. For cases of large permittivity, we also use a discretization of 20 points per wavelength to ensure accuracy. Numerical results of soil surfaces indicate that the TM backscattering is larger than TE. The difference

Manuscript received April 25, 1997; revised September 22, 1997. This work was supported in part by the National Science Foundation under contract ECS-9158040.

C. H. Chan is with the Applied Electromagnetics Laboratory, Department of Electronic Engineering, City University of Hong Kong, Kowloon, Hong Kong. He is also with the Electromagnetics and Remote Sensing Laboratory, Department of Electrical Engineering, University of Washington, Seattle, WA 98195 USA.

L. Tsang and Q. Li are with the Electromagnetics and Remote Sensing Laboratory, Department of Electrical Engineering, University of Washington, Seattle, WA 98195 USA.

Publisher Item Identifier S 0018-926X(98)01042-4.

increases as one gets closer to grazing. The difference also increases when the relative permittivity increases. The results are compared with the small perturbation method (SPM). The numerical results are significantly different from that of SPM due to multiple scattering. Numerical simulation gives much larger backscattering coefficients and a much smaller TM to TE ratio of backscattering than SPM. For the case of larger rms height, we also use additional horizontal surfaces that allow us to limit the bandwidth of the near interaction terms.

II. Integral Equation Formulation

The scattered field from a penetrable rough surface can be solved using coupled integral equations. If the fields on either side of the surface S are denoted by Ψ_1 and Ψ_2, respectively, for medium 1 and medium 2, they satisfy the following equation [19]:

$$h_1\Psi_i(\mathbf{r}) = h_2\Psi_{\text{in}}(\mathbf{r}) + \int_S \left[\Psi_i(\mathbf{r}')\,\frac{\partial G_i(\mathbf{r},\,\mathbf{r}')}{\partial \mathbf{n}'} - G_i(\mathbf{r},\,\mathbf{r}')\,\frac{\partial \Psi_i(\mathbf{r}')}{\partial \mathbf{n}'}\right] d\mathbf{r}' \quad (1)$$

$h_1 = 0.5$ and $h_2 = 1$ when $i = 1$; $h_1 = -0.5$ and $h_2 = 0$ when $i = 2$; where $\int_S$ denotes a Cauchy integral and G_i is the Green's function of the ith medium. Functions Ψ_1 and Ψ_2 are related through the boundary conditions on the surface S, namely

$$\Psi_1(\mathbf{r}) = \Psi_2(\mathbf{r}) \quad \text{and} \quad \frac{d\Psi_1(\mathbf{r})}{d\mathbf{n}} = \frac{1}{\rho}\,\frac{d\Psi_2(\mathbf{r})}{d\mathbf{n}} \quad (2)$$

where ρ equals μ_2/μ_1 and $\varepsilon_2/\varepsilon_1$ for TE and TM polarization, respectively. Applying the boundary conditions in conjunction with the collocation method, we arrive at a matrix equation

$$\Psi_{\text{in}}(x_m) = \sum_{n=1}^{N} a_{mn}F_1(x_n) + \sum_{n=1}^{N} b_{mn}F_2(x_n) \quad (3)$$

$$0 = \sum_{n=1}^{N} c_{mn}F_1(x_n) - \sum_{n=1}^{N} \rho d_{mn}F_2(x_n) \quad (4)$$

where $F_1(x) = \Psi_1(x)$ and $F_2(x) = \sqrt{1+[f'(x)]^2}\,(\partial\Psi_1/\partial n)$, respectively, and $x_m = (m - 0.5)\Delta x - L/2$. Function $f(x)$ represents the surface height at location x. For completeness, the matrix elements a_{mn}, b_{mn}, c_{mn}, and d_{mn} [17] are given here: for $m \neq n$

$$a_{mn} = \Delta x\,\frac{ik_1}{4}\,\frac{(x_m - x_n)f'(x_n) - [f(x_m) - f(x_n)]}{r_{mn}} \cdot H_1^{(1)}(k_1 r_{mn}) \quad (5)$$

$$b_{mn} = \Delta x\,\frac{i}{4}\,H_o^{(1)}(k_1 r_{mn}) \quad (6)$$

$$c_{mn} = -\Delta x\,\frac{ik_2}{4}\,\frac{(x_m - x_n)f'(x_n) - [f(x_m) - f(x_n)]}{r_{mn}} \cdot H_1^{(1)}(k_2 r_{mn}) \quad (7)$$

$$d_{mn} = \Delta x\,\frac{i}{4}\,H_o^{(1)}(k_2 r_{mn}). \quad (8)$$

where $r_{mn} = \sqrt{(x_m - x_n)^2 + [f(x_m) - f(x_n)]^2}$ and k_1 and k_2 are the wavenumbers in Region 1 and 2, respectively: for $m = n$

$$a_{mm} = \frac{1}{2} - \frac{f''(x_m)\Delta x}{4\pi\gamma_m^2} \quad (9)$$

$$b_{mm} = \Delta x\,\frac{i}{4}\,H_o^{(1)}[k_1\Delta x\gamma_m/(2e)] \quad (10)$$

$$c_{mm} = \frac{1}{2} + \frac{f''(x_m)\Delta x}{4\pi\gamma_m^2} \quad (11)$$

$$d_{mm} = \Delta x\,\frac{i}{4}\,H_o^{(1)}[k_2\Delta x\gamma_m/(2e)] \quad (12)$$

where $\gamma_m = \sqrt{1+[f'(x_m)]^2}$, $e = 2.718\,281\,83$, $f'(x_m)$, and $f''(x_m)$ represent the first and second derivative of $f(x)$ evaluated at x_m, respectively. Note that when the dielectric is lossy, c_{mn} and d_{mn} involve evaluations of Hankel functions with complex argument.

In the conventional matrix solution, F_2 is eliminated in (3) through the relation in (4). However, such elimination is not possible for an iterative solution for a large-scale problem. In an earlier implementation of the BMIA for the penetrable case without the use of FFT's [20], the two sets of unknowns F_1 and F_2 are labeled alternately along the 1-D surface discretized with N sample points resulting in the matrix equation as shown in (13) at the bottom of the page.

This will effectively double the required bandwidth of the stored near-interaction terms for the original BMIA approach. In this paper, we arrange the matrix equation as in (3) and (4) as shown in (14) at the bottom of the next page.

Similar to the BMIA/CG method, the strong near-interaction terms of the submatrices $[a]$, $[b]$, $[c]$, and $-\rho[d]$ are computed and stored while the weak far-interactions are computed by FFT's upon Taylor series expansion of the Green's function kernels. Note that the submatrices $[a]$ and $[c]$ are not symmetric while $[b]$ and $-\rho[d]$ are. The stored portion of the matrix is

$$\begin{bmatrix} a_{11} & b_{11} & a_{12} & b_{12} & \cdots & \cdots & a_{1N} & b_{1N} \\ c_{11} & -\rho d_{11} & c_{12} & -\rho d_{12} & \cdots & \cdots & c_{1N} & -\rho d_{1N} \\ \vdots & \vdots & \vdots & \vdots & \ddots & \ddots & \vdots & \vdots \\ a_{N1} & b_{N1} & a_{N2} & b_{N2} & \cdots & \cdots & a_{NN} & b_{NN} \\ c_{N1} & -\rho d_{N1} & c_{N2} & -\rho d_{N2} & \cdots & \cdots & c_{NN} & -\rho d_{NN} \end{bmatrix} \begin{bmatrix} F_1(x_1) \\ F_2(x_1) \\ \vdots \\ F_1(x_N) \\ F_2(x_N) \end{bmatrix} = \begin{bmatrix} \Psi_{\text{in}}(x_1) \\ 0 \\ \vdots \\ \Psi_{\text{in}}(x_N) \\ 0 \end{bmatrix} \quad (13)$$

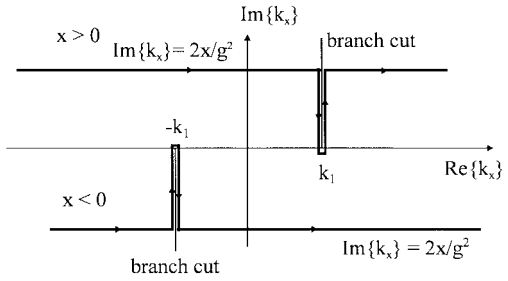

Fig. 1. Integration contour for the incident filed.

denoted by the shaded region as shown in

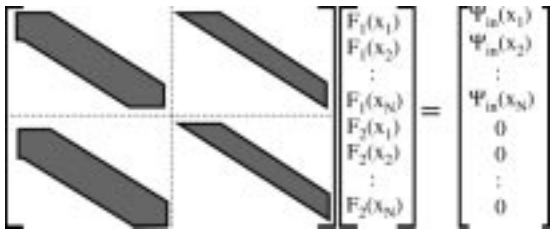

(15)

Equation (14) is to be solved by using the conjugate gradient method [21]. The incident field at the point $[x,\ f(x)]$ on the surface is given by

$$\Psi_{\text{in}}[x,\ f(x)] = \frac{g}{2\sqrt{\pi}} \int_{-\infty}^{\infty} dk_x e^{i(k_x x - k_z z)} e^{-[(k_x - k_{ix})^2 g^2/4]} \tag{16}$$

where $k_{ix} = k_1 \sin\theta_i$, $k_z^2 = k_1^2 - k_x^2$ with a proper choice of the branch cut, k_1 is the wavenumber of the incident field and an $e^{-i\omega t}$ convention is used. The advantage of (16) is that it obeys the wave equation exactly. To facilitate numerical evaluation of (16), a complex contour integration parallel to $\text{Re}\{k_x\}$ axis is carried out with $\text{Im}\{k_x\} = 2x/g^2$ and indentations are made for the vertical branch cuts at $k_x = \pm k_1$. Here g is the parameter that controls the tapering of the incident wave. The deformed contour is shown in Fig. 1. Note that the integration contours for $x > 0$ and $x < 0$ are different. The contours are chosen so that the integrals converge rapidly.

III. Taylor Series Expansion of Green's Function Kernels

The use of the FFT's to compute the nonnear interaction of the matrix–vector multiplication in solving (14) with an iterative procedure is similar to the procedure described in [18], which addressed the TE incidence and will not be repeated here. We would, however, include Taylor series expansion of the Green's function kernel for both the $H_0^{(1)}$ and $H_1^{(1)}$ here. For the Hankel function of the zeroth order we have

$$H_0^{(1)}\left(k\sqrt{x_d^2 + z_d^2}\right) = \sum_{m=0} a_m(x_d)\left(\frac{z_d}{x_d}\right)^{2m} \tag{17}$$

where $x_d = (x - x')$ and $z_d = (z - z') = f(x) - f(x')$. The first three terms of the expansion coefficients are given as

$$a_0(x_d) = H_0^{(1)}(kx_d) \tag{18}$$

$$a_1(x_d) = -H_1^{(1)}(kx_d)\frac{kx_d}{2} \tag{19}$$

$$a_2(x_d) = H_1^{(1)}(kx_d)\frac{kx_d}{4} - H_0^{(1)}(kx_d)\frac{(kx_d)^2}{8}. \tag{20}$$

For the Hankel function of the first order we have

$$\frac{H_1^{(1)}\left(k\sqrt{x_d^2 + z_d^2}\right)}{\sqrt{x_d^2 + z_d^2}} = \sum_{m=0} a_m(x_d) z_d^{2m}. \tag{21}$$

The first three terms of the expansion coefficients are given as

$$a_0(x_d) = \frac{H_1^{(1)}(kx_d)}{x_d} \tag{22}$$

$$a_1(x_d) = \frac{0.5kx_d H_0^{(1)}(kx_d) - H_1^{(1)}(kx_d)}{x_d^3} \tag{23}$$

$$a_2(x_d) = \frac{8H_1^{(1)}(kx_d) - 4kx_d H_0^{(1)}(kx_d) - k^2 x_d^2 H_1^{(1)}(kx_d)}{8x_d^5}. \tag{24}$$

The accuracy of the Taylor series expansion depends on the ratio of z_d/x_d, which in turn dictates the bandwidth of the stored near interactions as shown in the shaded region of (15). For random surfaces of large rms heights, Taylor series expansion about the canonical grid point of $z = 0$ is not sufficient. Instead, Taylor series expansion about several canonical grid points or multiple flat surfaces may be required. Fig. 2 shows the canonical grids for the modified Taylor series expansion. Note that $[x_i,\ z_{io}]$ lies on a flat surface with $f(x_i) = m\Delta z$. The Taylor series expansion about a multiple flat surface is given as

$$\begin{aligned} H(kr) \cong\ & z_{di}^0(g_0 z_{dj}^0 + g_1 z_{dj}^1 + g_0 z_{dj}^2/2 + g_0 z_{dj}^3/6) \\ & + z_{di}^1(g_1 z_{dj}^0 + g_2 z_{dj}^1 + g_3 z_{dj}^2/2) \\ & + z_{di}^2(g_2 z_{dj}^0 + g_3 z_{dj}^1)/2 + z_{di}^3(g_3 z_{dj}^0)/6. \end{aligned} \tag{25}$$

$$\begin{bmatrix} a_{11} & a_{12} & \cdots & a_{1N} & b_{11} & b_{12} & \cdots & b_{1N} \\ a_{21} & a_{22} & \cdots & a_{2N} & b_{21} & b_{22} & \cdots & b_{2N} \\ \vdots & \vdots & \ddots & \vdots & \vdots & \vdots & \ddots & \vdots \\ a_{N1} & a_{N2} & \cdots & a_{NN} & b_{N1} & b_{N2} & \cdots & b_{NN} \\ c_{11} & c_{12} & \cdots & c_{1N} & -\rho d_{11} & -\rho d_{12} & \cdots & -\rho d_{1N} \\ c_{21} & c_{22} & \cdots & c_{2N} & -\rho d_{21} & -\rho d_{22} & \cdots & -\rho d_{2N} \\ \vdots & \vdots & \ddots & \vdots & \vdots & \vdots & \ddots & \vdots \\ c_{N1} & c_{N2} & \cdots & c_{NN} & -\rho d_{N1} & -\rho d_{N2} & \cdots & -\rho d_{NN} \end{bmatrix} \begin{bmatrix} F_1(x_1) \\ F_1(x_2) \\ \vdots \\ F_1(x_N) \\ F_2(x_1) \\ F_2(x_2) \\ \vdots \\ F_2(x_N) \end{bmatrix} = \begin{bmatrix} \Psi_{\text{in}}(x_1) \\ \Psi_{\text{in}}(x_2) \\ \vdots \\ \Psi_{\text{in}}(x_N) \\ 0 \\ 0 \\ \vdots \\ 0 \end{bmatrix} \tag{14}$$

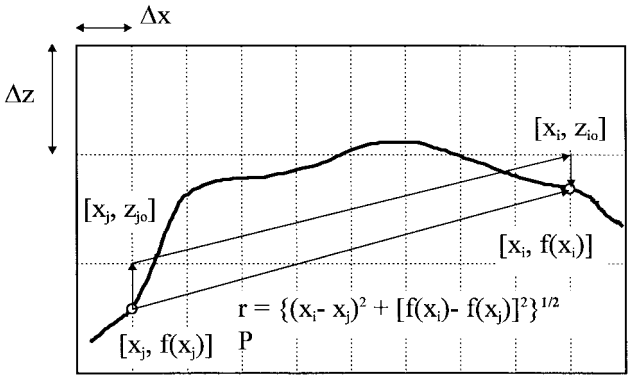

Fig. 2. Canonical grid for modified Taylor series expansion.

Here, H represents both $H_0^{(1)}$ and $H_1^{(1)}/r$, $g_n = \partial^n H(kr)/\partial z_{io}^n$, $z_{di}^n = (z_i - z_{io})^n$, and $z_{dj}^n = (z_{jo} - z_j)^n$. With this type of expansion, the bandwidth of the strong near-interaction can be reduced substantially. However, the tradeoff is that two-dimensional FFT's are required for the weak far-interaction computations. The optimal choice of bandwidth and number of canonical grid point requires extensive numerical experiments and will not be addressed here.

IV. Numerical Results and Discussion

In this section, we illustrate the numerical results of bistatic scattering and backscattering coefficients for different incidence angles and different polarizations using soil surfaces with various soil moisture contents. At L band (1.43 GHz), the relative permittivity of soil at soil moisture of 10, 15, 20, 25, and 30% are $5.56 + i0.6$, $10.8 + i1.335$, $17.7 + i2.26$, $24.6 + i3.185$, and $31.5 + i4.11$, respectively, [22]. For ease of reference, we have tabulated the parameters of the various number of cases that we have computed in Table I. For all the cases in this paper (except Fig. 3), the random rough surfaces are Gaussian random rough surfaces with given rms height $h = 0.2\lambda$ and correlation length $l = 0.6\lambda$. For the case of Fig. 3, we choose rms height $h = 0.05\lambda$ and correlation length $l = 0.3\lambda$. The tapering parameter is chosen at $g = L/8$ to ensure that the effects of edge diffraction is not important for the incident and scattering angles of interest.

First, we compare the results with the small perturbation method. Next, we illustrate the convergence test and CPU comparison. For a fixed incidence angle, the accuracy of the results can decrease with the increase of scattering angle toward $-90°$. An important criterion for all acceptable result is that it gives an accurate result in the vicinity of the backscattering direction. Then we illustrate and discuss the results of TE and TM backscattering for various parameters of interest. Finally, we compare the results of multilevel expansion with a single level.

A. Comparison Between Numerical Simulation and SPM for the Case of Small RMS Height and Slope

In Fig. 3, we compare the bistatic scattering coefficients for angles in the vicinity of backscattering direction of case with rms height 0.05 wavelength, correlation length 0.3 wavelength at incidence angle 80° between numerical simulation and SPM. For ready reference, the bistatic scattering coefficients of a 1-D dielectric rough surface obtained by the first-order small perturbation method are listed in the Appendix. For numerical simulation, we use a surface length of 200 wavelengths and the results were averaged over 50 realizations. The two results are in agreement for scattering angles between $-75°$ and $-85°$. For this case, kh is at a relatively small value of 0.31, so that multiple scattering effects become less important. Thus, the first-order SPM result is reasonably accurate.

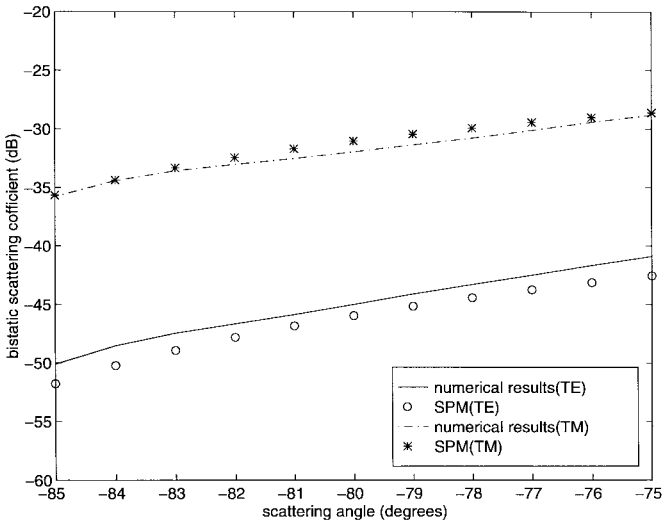

Fig. 3. Comparison of bistatic scattering coefficient at near backscattering direction between SPM and numerical simulation with the following parameters: rms $h = 0.05\lambda$, $l = 0.3\lambda$, $\theta_i = 80°$, $\varepsilon_r = 5.56 + i0.6$, $L = 200\lambda$, $g = L/8$, and number of realization = 50.

TABLE I
The Parameters for the Various Cases

case #	relative permittivity	surface length L in λ	# of surface unknowns	incident angle θ_i in degrees
1	5.56 + i0.6	500	10,000	80
2	5.56 + i0.6	200	4,000	80
3	5.56 + i0.6	500	10,000	85
4	5.56 + i0.6	1000	20,000	85
5	17.7 + i2.26	200	4,000	80
6	17.7 + i2.26	200	8,000	80

B. Convergence Test and CPU Comparison

1) Convergence with Respect to Surface Length and Number of Realizations: In Fig. 4, we compare the bistatic scattering coefficients at the near backscattering direction for Case 1 and Case 2 with permittivity of 10% soil moisture at an incidence angle 80°. We plot two results for Case 2. One is averaged over 50 realizations and the other is averaged over 100 realizations. The results indicate that there is little difference between 50 and 100 realizations for both TE and TM waves. This demonstrates convergence with respect to

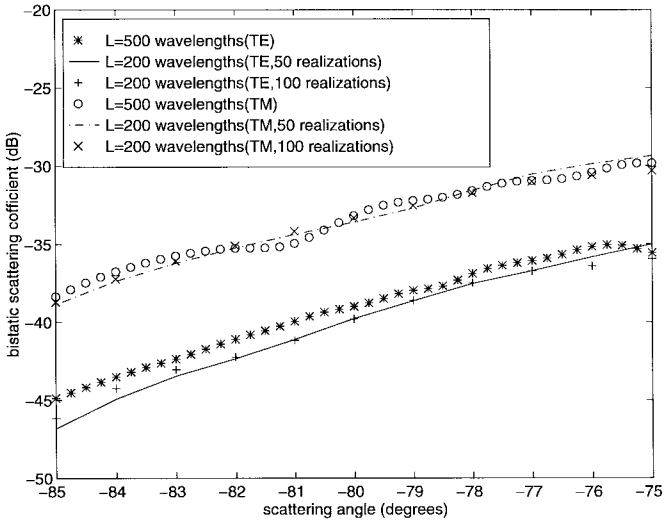

Fig. 4. Comparison of bistatic scattering coefficient at near backscattering direction between Case 1 and Case 2; rms $h = 0.2\lambda$, $l = 0.6\lambda$, $\theta_i = 80°$, $\varepsilon_r = 5.56 + i0.6$, $g = L/8$, and number of realization = 50 for $L = 500\lambda$.

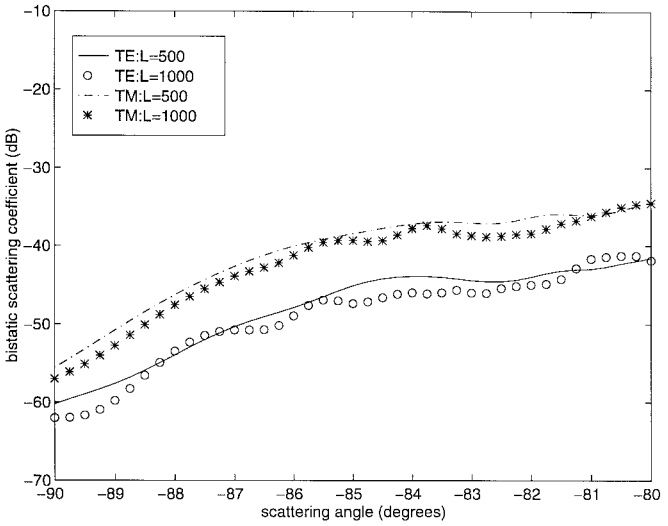

Fig. 5. Comparison of bistatic scattering coefficient at near backscattering direction between Case 3 and Case 4; rms $h = 0.2\lambda$, $l = 0.6\lambda$, $\theta_i = 85°$, $\varepsilon_r = 5.56 + i0.6$, $g = L/8$, and number of realization = 20.

realization. The differences between results of surface lengths 500 and 200 wavelengths are slightly bigger. Nevertheless, the differences at the backscattering angle of $\theta_s = -80°$ are only 0.78 dB for TE and 0.74 dB for TM. This indicates that a 200 wavelength surface length is large enough for an incidence angle of 80°. In Fig. 5, we show convergence with respect to surface length at an 85° incidence angle using 1000 and 500 wavelengths of surface length. The two results are in agreement at backscattering of $\theta_s = -85°$. This shows that surface length of 500 wavelengths is large enough for an incidence angle of 85°.

2) Convergence with Respect to Number of Sampling Points per Wavelength: For problems of high soil moisture, the relative permittivity can be more than $31.5 + i4.11$. It may become necessary to use a sampling of more than 10 points per

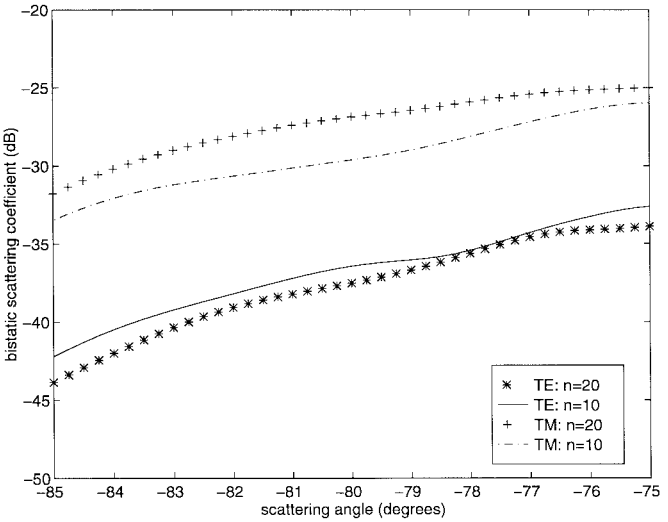

Fig. 6. Comparison of bistatic scattering coefficient at near backscattering direction between Case 5 and Case 6; rms $h = 0.2\lambda$, $l = 0.6\lambda$, $\theta_i = 80°$, $\varepsilon_r = 17.7 + i2.26$, $g = L/8$, $L = 200\lambda$, and number of realization = 50.

TABLE II
THE CPU AND MEMORY REQUIREMENTS FOR ONE REALIZATION

case #	CPU time (seconds)	memory(Mbytes)
1	347 (TE*), 191 (TM*)	50.2
2	119 (TE), 74 (TM)	19.5
3	279 (TE), 258 (TM)	50.2
4	795 (TE), 522 (TM)	19.5

wavelength. In Fig. 6, we provide the comparison of using 10 points per wavelength versus 20 points per wavelength for 50 realizations with a surface length 200 wavelengths and relative permittivity $17.7 + i2.26$. The backscattering results are about 1.08 dB different for TE wave and 2.75 dB different for TM wave. This indicates that 20 points or more per wavelength should be used if more accurate results are desired, particularly for TM waves. This is because most of the incident wave was transmitted to a lower medium of high permittivity for the TM case and was scattered to the upper medium for the TE case.

3) Comparison of CPU Time and Memory Requirements: Sample results are performed using an Alpha Server 4100. The CPU and memory requirements for one realization are tabulated in Table II. The indicated CPU time and memory are much lower than that of using direct matrix inversion. Actually, the use of direct matrix inversion is not workable on the Alpha Server because of the large memory requirement for 10 000 surface unknowns. Using the method in this paper, the case of 10 000 surface unknowns only requires a CPU time of about 6 min for TE and 3 min for TM for one realization.

C. Variation of Backscattering Coefficients with Soil Moisture Contents and Comparison with SPM

In Fig. 7, we plot the backscattering coefficients as a function of soil moisture contents at an incidence angle of 80°. For the case of a surface with soil moisture of 10 and 15%, we

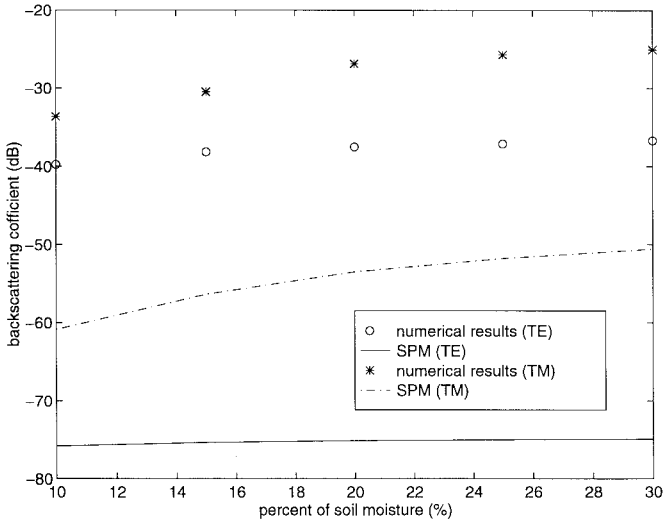

Fig. 7. Comparison of the variation of backscattering coefficients with percent of soil moisture contents between numerical simulation and SPM; rms $h = 0.2\lambda$, $l = 0.6\lambda$, $\theta_i = 80°$, $g = L/8$, $L = 200\lambda$, and number of realization $= 50$.

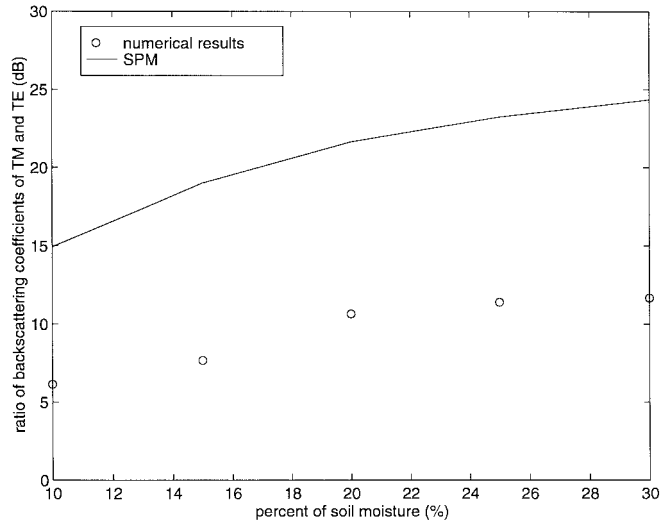

Fig. 8. Variation of ratio of backscattering coefficients of TM and TE with percent of soil moisture contents and comparison with SPM; rms $h = 0.2\lambda$, $l = 0.6\lambda$, $\theta_i = 80°$, $g = L/8$, $L = 200\lambda$, and number of realization $= 50$.

use 10 points per wavelength and 20 points per wavelength for other cases because of the large relative permittivity. The results are tabulated in Table III for better quantitative comparisons. We also show the SPM results for comparison. We note that as soil moisture increases, the backscattering coefficients increases. They have a large increase at small moisture. The rate of increase levels off at high soil moisture. In Fig. 8, we plot the ratio of TM to TE backscattering as a function of soil moisture. We note that TM backscattering is much larger than TE backscattering. The ratio also increases as a function of soil moisture. This shows that the ratio of TM to TE backscattering can be an important indicator of soil moisture in remote sensing applications. The comparison with SPM results show that the latter are erroeous. SPM gives much

TABLE III
BISTATIC SCATTERING COEFFICIENT AT BACKSCATTERING ANGLE AS A FUNCTION OF THE PERCENT OF SOIL MOISTURE

percent of soil moisture (%)	relative dielectric constant	TE (Num.*)	TM (Num.)	Ratio** (Num.)	TE (SPM***)	TM (SPM)	Ratio (SPM)
10	5.56 + i0.6	-39.78	-33.64	6.14	-75.80	-60.89	14.92
15	10.8 + i1.335	-38.15	-30.48	7.67	-75.36	-56.36	19.00
20	17.7 + i2.26	-37.52	-26.87	10.65	-75.13	-53.49	21.64
25	24.6 + i3.185	-37.12	-25.72	11.40	-75.02	-51.78	23.23
30	31.5 + i4.11	-36.70	-25.02	11.68	-74.94	-50.59	24.35

* Numerical simulation results

** Ratio of the bistatic scattering coefficient at backscattering angle of TM and TE waves

*** Results by using small perturbation method

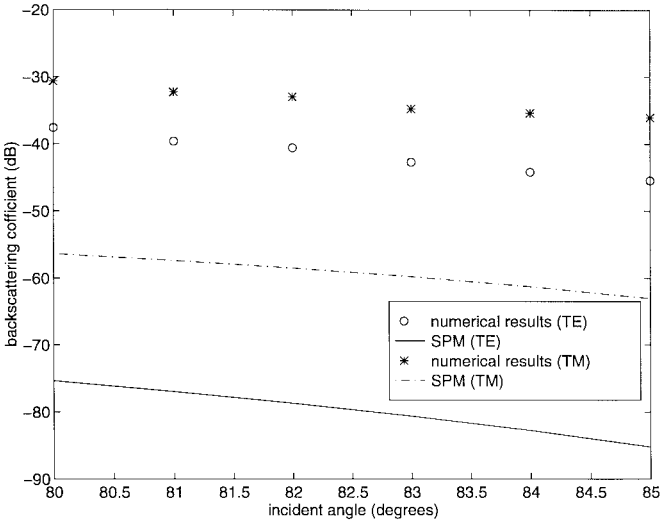

Fig. 9. Comparison of the variation of backscattering coefficients with incident angles between numerical simulation and SPM; rms $h = 0.2\lambda$, $l = 0.6\lambda$, $\varepsilon_r = 10.8 + i1.335$, $g = L/8$, $L = 500\lambda$, and number of realization $= 50$.

lower backscattering coefficients and also a much larger ratio of TM to TE backscattering than numerical simulations.

D. Variation of Backscattering Coefficients with Incidence Angles and Comparison with SPM

In Fig. 9, we plot the TE and TM backscattering coefficients as a function of incidence angle from 80° to 85°. To ensure accurate results, we have used a surface length of 500 wavelengths. The results are also tabulated in Table IV for better quantitative comparisons. The ratio of TM to TE backscattering is plotted in Fig. 10. Both TE and TM backscattering decreases as a function of incidence angle. However, the ratio of TM to TE backscattering increases with incidence angle. Again the SPM gives much larger ratio than numerical simulations.

E. Comparing Results of Multilevel Expansion with a Single Level

In Fig. 11, we compare the results of the BMIA/CG method with the multiple-level expansion method for one realization

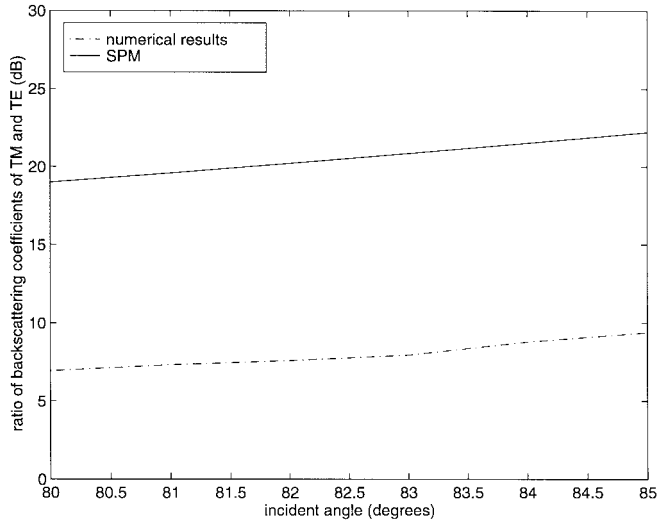

Fig. 10. Variation of ratio of backscattering coefficients of TM and TE with incident angles and comparison with SPM; rms $h = 0.2\lambda$, $l = 0.6\lambda$, $\varepsilon_r = 10.8 + i1.335$, $g = L/8$, $L = 500\lambda$, and number of realization = 50.

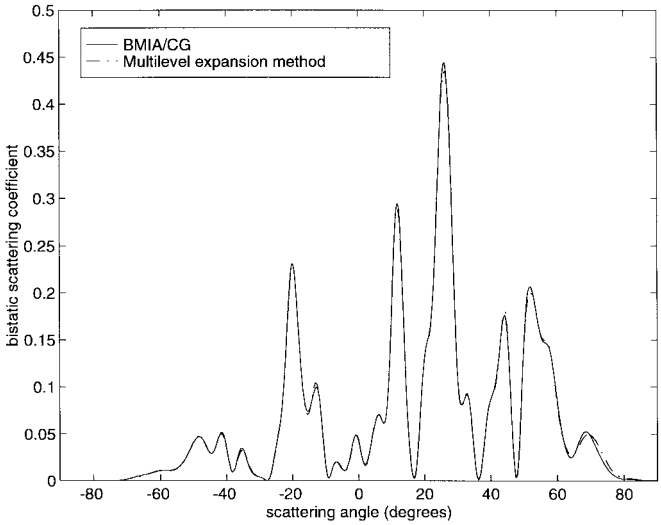

Fig. 11. Comparison of bistatic scattering coefficients using BMIA/CG and multilevel expansion method for one realization. TE wave; rms $h = 0.2\lambda$, $l = 0.6\lambda$, $\theta_i = 45°$, $\varepsilon_r = 5.56 + i0.6$, $g = L/8$, $L = 50\lambda$, BMIA/CG half-bandwidth $b = 200$ (20 wavelengths), multilevel expansion half-bandwidth $b = 50$ (five wavelengths).

TABLE IV
BISTATIC SCATTERING COEFFICIENT AT BACKSCATTERING ANGLE AS A FUNCTION OF THE INCIDENT ANGLE

incident angle (degrees)	TE (Num.)	TM (Num.)	Ratio (Num.)	TE (SPM)	TM (SPM)	Ratio (SPM)
80	-37.598	-30.668	6.93	-75.36	-56.36	18.99
81	-39.615	-32.270	7.326	-76.97	-57.39	19.59
82	-40.567	-32.97	7.594	-78.72	-58.51	20.20
83	-42.704	-34.76	7.946	-80.63	-59.78	20.84
84	-44.160	-35.37	8.787	-82.78	-61.26	21.52
85	-45.440	-36.04	9.400	-85.25	-63.03	22.22

with rms height 0.2 wavelength, correlation length 0.6 wavelength, surface length 50 wavelengths, and relative permittivity $5.56 + i0.6$ at an incidence angle of 45°. The two results are in good agreement. The half-bandwidth used for BMIA/CG is 20 wavelengths. The half-bandwidth used for the multiple-level expansion is five wavelengths. This indicates that the multiple-level expansion is useful for cases with larger rms height, as it accommodates a substantially smaller bandwidth.

V. CONCLUSIONS

In this paper, we have modified the BMIA/CG method to perform Monte Carlo simulations of random penetrable surfaces. The method permits the solution of low-grazing backscattering problems with large surface lengths at modest CPU requirements. Numerical results of soil surfaces indicate that the TM backscattering is larger than TE. The ratio of TM to TE backscattering increases as one gets closer to grazing. The ratio also increases when the relative permittivity increases. Comparing with first-order SPM indicates that the latter can be erroneous by many decibels.

APPENDIX

The bistatic scattering coefficients of a 1-D dielectric rough surface with Gaussian power spectrum using small perturbation method are

$$\sigma_{aa}(\theta_s) = 4k^3 \cos^2\theta_s \cos\theta_i f_{aa} W(k_{1x} - k_{1xi})$$

where

$$f_{hh} = \left| \frac{k_2^2 - k_1^2}{(k_{2z} + k_{1z})(k_{2zi} + k_{1zi})} \right|^2$$

$$f_{vv} = \left| \frac{k_2^2 - k_1^2}{(k_2^2 k_{1z} + k_1^2 k_{2z})(k_2^2 k_{1zi} + k_1^2 k_{2zi})} \cdot [k_2^2 k_1^2 \sin\theta_s \sin\theta_i - k_1^2 k_{2z} k_{2zi}] \right|^2$$

$$W(k_x) = \frac{h^2 l}{2\sqrt{\pi}} \exp\left(-\frac{k_x^2 l^2}{4}\right)$$

and

$$k_{1zi} = k_1 \cos\theta_i, \quad k_{1xi} = k_1 \sin\theta_i, \quad k_{1x} = k_1 \sin\theta_s$$

$$k_{2zi} = \sqrt{k_2^2 - k_{1xi}^2}, \quad k_{2z} = \sqrt{k_2^2 - k_{1x}^2}.$$

REFERENCES

[1] C. L. Rino and H. D. Ngo, "Application of beam simulation to scattering at low grazing angles—Pt. 2: Oceanlike surfaces," *Radio Sci.*, vol. 29, no. 6, pp. 1381–1391, Nov. 1994.
[2] D. A. Kapp and G. S. Brown, "A new numerical method for rough-surface scattering calculations," *IEEE Trans. Antennas Propagat.*, vol. 44, pp. 711–721, May 1996.
[3] D. Holliday, L. L. DeRead, Jr., and G. J. St-Cyr, "Forward–backward: A new method for computing low-grazing angle scattering," *IEEE Trans. Antennas Propagat.*, vol. 44, pp. 722–729, May 1996.
[4] A. G. Voronovich, *Wave Scattering From Rough Surfaces.* Berlin, Germany: Springer-Verlag, 1994.
[5] R. M. Axline and A. K. Fung, "Numerical computation of scattering from a perfectly conducting random surface," *IEEE Trans. Antennas Propagat.*, vol. AP-26, pp. 482–488, May 1978.
[6] A. A. Maradudin, E. R. Mendez, and T. Michel, "Backscattering effects in the elastic scattering of p-polarization light from a large amplitude random grating," in *Scattering in Volumes and Surfaces*, M. Nieto-Vesperians and J. C. Dainty, Eds. North-Holland, The Netherlands: Elsevier, 1990.

[7] E. I. Thorsos, "The validity of the Kirchhoff approximation for rough surface scattering using a Gaussian roughness spectrum," *J. Acoust. Soc. Amer.*, vol. 83, pp. 78–92, 1988.
[8] J. S. Chen and A. Ishimaru, "Numerical simulation of the second order Kirchhoff approximation from very rough surfaces and study of backscattering enhancement," *J. Acoust. Soc. Amer.*, vol. 88, pp. 1846–1850, 1990.
[9] M. Nieto-Vesperinas and J. M. Soto-Crespo, "Monte Carlo simulations for scattering of electromagnetic waves from perfectly conducting random rough surfaces," *Opt. Lett.*, vol. 12, pp. 979–981, 1987.
[10] C. Rino, T. Crystal, A. Koide, H. Ngo, and H. Guthart, "Numerical simulations of backscatterer from linear and nonlinear ocean surface realization," *Radio Sci.*, vol. 26, pp. 51–72, 1992.
[11] Y. Kim, E. Rodriguez, and S. Durden, "A numerical assessment of rough surface scattering theories: Vertical polarization," *Radio Sci.*, vol. 27, pp. 515–527, 1992.
[12] D. Maystre, M. Saillard, and J. Ingers, "Scattering by one- or two-dimensional randomly rough surfaces," *Waves Random Media*, vol. 1, pp. 143–155, 1991.
[13] R. Chen and J. C. West, "Analysis of scattering from rough surface at large incidence angles using a periodic-surface moment method," *IEEE Trans. Geosci. Remote Sensing*, vol. 33, pp. 1206–1213, Sept. 1995.
[14] L. Tsang, C. H. Chan, and H. Sangani, "A banded matrix iterative approach to Monte Carlo simulations of scattering of waves by large-scale random rough surface problems: TM case," *Electron. Lett.*, vol. 29, no. 2, pp. 166–167, Jan. 1993.
[15] L. Tsang, C. H. Chan, H. Sangani, A. Ishimaru, and P. Phu, "A banded matrix iterative approach to Monte Carlo simulations of large-scale random rough surface scattering: TE case," *J. Electromagn. Waves Applicat.*, vol. 7, no. 9, pp. 1185–1200, 1993.
[16] L. Tsang, C. H. Chan, K. Pak, and H. Sangani, "A BMIA/FFT algorithm for the Monte Carlo simulations of large scale random rough surface scattering: Application to grazing incidence," in *IEEE Anntennas Propagat. Soc. Int. Symp.*, Seattle, WA, June 1994, vol. 3, pp. 2028–2031.
[17] L. Li, C. H. Chan, and L. Tsang, "Numerical simulation of conical diffraction of tapered electromagnetic waves from random rough surfaces and applications to passive remote sensing," *Radio Sci.*, vol. 29, no. 3, pp. 587–598, May/June 1994.
[18] L. Tsang, C. H. Chan, K. Pak, and H. Sangani, "Monte Carlo simulations of large-scale problems of random rough surface scattering and applications to grazing incidence with the BMIA/canonical grid method," *IEEE Trans. Antennas Propagat.*, vol. 43, pp. 851–859, Aug. 1995.
[19] L. Tsang, J. A. Kong, and R. T. Shin, *Theory of Microwave Remote Sensing*. New York: Wiley, 1985.
[20] C. H. Chan, L. Li, and L. Tsang, "A banded matrix iteration approach to Monte Carlo simulation of large-scale random rough surface scattering: Penetrable case," in *Proc. 9th Annu. Rev. Progress Appl. Computat. Electromagn. Symp.*, Monterey, CA, Mar. 1993, pp. 391–397.
[21] C. H. Chan and R. Mittra, "Some recent development in iterative techniques for solving electromagnetic boundary value problems," *Radio Sci.*, vol. 22, pp. 929–934, 1987.
[22] T. J. Schmugge, T. Wilheit, W. Webster, Jr., and P. Gloersen, "Remote sensing of soil moisture with microwave radiometers, II," NASA TND-8321, Goddard Space Flight Ctr., Greenbelt, MD, 1976.

Chi Hou Chan received the Ph.D. degree in electrical engineering from the University of Illinois, Urbana, IL, in 1987.

From 1987 to 1989, he was a Visiting Assistant Professor at the University of Illinois associated with the Electromagnetic Communication Laboratory. He joined the Department of Electrical Engineering, University of Washington, Seattle, WA, in 1989 as an Assistant Professor. He was promoted to Associate Professor with tenure in 1993. Since April 1996 he has been with the Department of Electronic Engineering, City University of Hong Kong, where he is currently a Professor and the Director of Applied Electromagnetic Laboratory. His current research includes electronic packaging, remote sensing, and wireless communications.

Dr. Chan is a member of the US URSI, Commission B and a recipient of the 1991 US NSF Presidential Young Investigator Award. He is also a member of the Electromagnetic Academy.

Leung Tsang (S'73–M'75–SM'85–F'90) was born in Hong Kong. He received the B.S. degree, in 1971, the M.S. and E.E. degrees, in 1973, and the Ph.D. degree, in 1976, all from the Massachusetts Institute of Technology, Cambridge.

He is presently a Professor of electrical engineering at the University of Washington, Seattle. He was a Research Engineer with Schlumberger-Doll Research Center between 1976 and 1978. From 1980 to 1983 he was with the Department of Electrical Engineering and Remote Sensing Center, Texas A&M University, College Station. He is on the Editorial Board of the *Journal of Electromagnetic Waves and Applications* and was an Associate Editor of *Radio Science*. He is a co-author of the book *Theory of Microwave Remote Sensing* (New York: Wiley, 1985). His current research interests include wave propagation in random media and rough surfaces, remote sensing, and opto-electronics.

Dr. Tsang has been the Editor of IEEE TRANSACTIONS ON GEOSCIENCE AND REMOTE SENSING since 1996. He was the Technical Program Chairman of the 1994 IEEE Antennas and Propagation International Symposium and URSI Radio Science Meeting and the Technical Program Chairman of the 1995 Progress in Electromagnetics Research Symposium. He is the General Chairman of the 1998 IEEE International Geoscience and Remote Sensing Symposium. He is a Fellow of the Optical Society of America.

Qin Li received the B.S. and M.S. degrees in space physics in 1985 and 1988, respectively, from Wuhan University, P.R. China. He is currently working toward the Ph.D. degree in electrical engineering from the University of Washington, Seattle.